Journal of *Marine Science and Engineering*

MDPI

Article

Experimental Investigation on Structural Responses of a Partially Submerged 2D Flat Plate with Hammering and Breaking Waves for Numerical Validation

Yoon-Jin Ha, Byoung-Jae Park, Yun-Ho Kim * and Kang-Su Lee

Korea Research Institute of Ships and Ocean Engineering, Deajeon 34103, Korea; yj_ha0811@kriso.re.kr (Y.-J.H.); byoungjae@kriso.re.kr (B.-J.P.); klee@kriso.re.kr (K.-S.L.)

* Correspondence: yunhokim@kriso.re.kr; Tel.: +82-42-866-3959

Abstract: In this study, experiments were conducted to provide validation data for numerical simulations. Model tests were conducted in a 2D wave flume at the Korea Research Institute of Ships and Ocean Engineering (KRISO). A series of hammering tests for two flat plates with different lengths under dry and partially wet conditions were performed to investigate the vibrating frequencies in each mode. Thereafter, breaking wave tests were performed using the focusing wave method. Repetitive tests were performed five times in each condition. The repetitive test results showed good agreement in each case, and the frequencies for each mode of the two flat plates were numerically calculated. In addition, the wave and air bubble frequencies were captured unlike in the hammering tests. The frequencies for each mode, strain and time interval from the experiments for two flat plates were organized, and the data for validation of the numerical simulation were provided.

Keywords: 2D partially submerged flat plate; fluid-structure interaction; vibrating frequency; hammering test; breaking wave test

check for updates

Citation: Ha, Y.-J.; Park, B.-J.; Kim, Y.-H.; Lee, K.-S. Experimental Investigation on Structural Responses of a Partially Submerged 2D Flat Plate with Hammering and Breaking Waves for Numerical Validation. *J. Mar. Sci. Eng.* **2021**, *9*, 621. https://doi.org/10.3390/jmse9060621

Academic Editor: Fuping Gao

Received: 6 May 2021
Accepted: 2 June 2021
Published: 3 June 2021

Publisher's Note: MDPI stays neutral with regard to jurisdictional claims in published maps and institutional affiliations.

Copyright: © 2021 by the authors. Licensee MDPI, Basel, Switzerland. This article is an open access article distributed under the terms and conditions of the Creative Commons Attribution (CC BY) license (https://creativecommons.org/licenses/by/4.0/).

1. Introduction

The fluid-structure interaction of a large structure, such as a very large floating structure (VLFS), a large container ship, is an important problem in the design phase. Moreover, the hydroelasticity response can occur on a large structure through interaction with the fluid. The hydroelasticity response effect is largely related to structural deformation (Newman [1]), and the structural deformation is related to a wave impact problem.

The wave impact loads can include dynamic loading due to a dynamic response on a structure, thus, many researchers have demonstrated wave impact loads by breaking waves. Furthermore, it is well known that the breaking wave impact load is relatively higher than a non-breaking wave impact load at the same wave height (Kjeldsen et al. [2], Basco and Niedzwecki [3], Hong and Shin [4]).

Previously, wave impact loads were estimated from analytical solutions, which were suggested by von Karman [5], Wagner [6], and Goda et al. [7]. However, the analytical solutions can be used only for structures with simple shapes; however, they cannot be considered as breaking wave condition. Therefore, experimental and computational fluid dynamic (CFD) studies are essential for the estimation of the breaking wave impact load.

In the laboratory, Hattori et al. [8], Chan et al. [9], Wienke et al. [10] and Ha et al. [11] estimated the breaking wave impact loads on a vertical wall and a vertical circular cylinder. Huang et al. [12] measured breaking wave impact loads on a gravity-based structure (GBS) model, and they showed mechanical vibrations and air bubble effects in time histories of wave impact loads. For mechanical vibration, they explained that the vibration is dominantly affected by the relationship between the natural frequency of the sensor and the sampling rate. Jose and Choi [13] performed a study to modify the slamming coefficients. They performed experiments and numerical simulations for breaking wave impact loads

on a jacket platform, and recommended the maximum slamming coefficients for bracing and vertical members. Similarly, Ha et al. [14] studied the slamming coefficients and performed model tests for bow-flare slamming of a ship-type FPSO (Floating Production Storage and Offloading) under irregular waves. They showed that the experimental results were larger than the slamming coefficients reported by Chuang [15]. Until recently, the mechanism of breaking wave generation, its observations, and interactions between breaking waves and structures were experimentally investigated in two-dimensional wave flumes (Moragues et al. [16], Li et al. [17], Escudero et al. [18]).

Regarding the CFD study, Khayyer and Gotoh [19] computed slamming impact loads on a vertical wall using the moving particle semi-implicit (MPS) method, and they demonstrated the air compressibility of slamming impact pressures. Liu et al. [20] studied wave interaction with a porous structure using the volume-of-fluid (VOF) method. Their CFD results were directly compared with the model test results, and the numerical results were in good agreement with the model test results. Kamath et al. [21] and Ha et al. [22] computed breaking wave impact loads according to the breaking locations of incoming waves. They used the level-set method (LSM) and VOF method, respectively. Generally, numerical results are compared with the experimental results. However, most experimental and numerical studies have used rigid models.

Sometimes hydroelasticity need to be considered in wave impact problems. Popular analytical methods for hydroelasticitiy include: the modal superposition method and direct method. For the model superposition method, modes of rigid and elastic bodies are calculated, and hydroelasticity deformation is calculated by superposing the elasticity response (Newman [1]). In addition, the modal superposition method can be applied in dry and wet modes, and be used for frequency (Fu et al. [23]; Hamamoto and Fujita [24]; Wu et al. [25]) and time (Malenica et al. [26]; Kara [27]; Rajendran and Guedes [28] domain methods. Fu et al. [23] predicted the hydroelasticity response of flexible floating interconnected structures using the dry mode method. They showed the effects of the connector and module stiffness on the hydroelasticity response. Senjanović et al. [29] showed a unique formulation for restoring stiffness using the dry mode method. For the wet mode method, the added mass and restoring stiffness are additionally considered in the modal analysis. Loukogeorgaki et al. [30] and Michailides et al. [31] calculated the hydroelasticity of a flexible barge shape under oblique waves. Humamoto and Fujita [24] demonstrated the hydroelasticity response of a large floating structure using the wet mode method. Moreover, they demonstrated the accuracy and effectiveness of the hybrid model of the boundary element method (BEM) and finite element method (FEM). For the direct method, FEM is mainly coupled with CFD; thus the analysis time is relatively long. However, the direct method can consider the non-linearity. Fourey et al. [32]; Li et al. [33]; Liu and Zhang [34], and Sun et al. [35] used Lagrangian codes, such as the smooth particle method (SPH), MPS, as hydrodynamic simulations. Izadi et al. [36] and Liao et al. [37] used Eulerian codes. For the Lagrangian code, nodes in the FEM are matched with each particle, while for the Eulerian code, a mesh in the FEM is overlapped on the mesh of a body. Therefore, it is necessary to interpolate data between meshes of the FEM and Eulerian code.

In addition, to capture the interaction between structures and fluid, well-known methods are widely used such as the arbitrary Lagrangian Eulerian (ALE) method (Donea et al. [38]; Hirt et al. [39]; Hughes et al. [40]; Hu et al. [41]), the immersed boundary method (Peskin and McQueen [42]; Dillon and Fauci [43]; Gilmanov and Sotiropoulos [44]; Zhu and Peskin [45]; Nestola et al. [46]; Griffith et al. [47]), and the fictitious domain method (Glowinski et al. [48]). In the case of the ALE method, the method allows arbitrary body motion of mesh points with respect to frame of reference. The immersed boundary method is a non-boundary fitting method, which is not required changes of mesh. Another method is the fictitious domain method, which is closely related to the immerged boundary method. The fictitious domain method was developed within finite difference and evolved from the finite element field (van Loon [49]).

To validate the modal superposition method and direct method, relatively simple experimental data are required; however most of the experiments were performed for segment models of container ships and other large floating bodies. As for the segment model, the number of segments with backbones and attachment of strain-gauges on the backbones are important because of bending and torsional natural frequencies (Kim et al. [50]). Therefore, many numerical simulations were compared with the water entry problems of rigid experimental models (Garabedian [51]; Judge et al. [52]; Bargasteh et al. [53]; Russo et al. [54]; Wang and Soares [55]). Thereafter, hydroelasticity problems were solved.

In this study, experiments were performed to validate the numerical analysis. The modes and natural frequencies of flat plates under dry and partially wet conditions were investigated using hammering tests, and deformations of the flat plates by strain-gauges were investigated under regular and breaking waves. The breaking wave was generated using the focusing wave method. From the experiments, the data for validation and snapshots were obtained.

2. Experimental Setup

2.1. Experimental Model

In this model test, flat plates with two different lengths, were installed in a 2D wave flume of the Korea Research Institute of Ships and Ocean Engineering (KRISO). As shown in Figure 1, the breadths and thicknesses of the two flat plates were 200 mm and 1 mm, respectively. In addition, the length of Model A is 250 mm (Figure 1a), and the length of Model B is 326 mm (Figure 1b). The bottom of Model A was located 38 mm above the water surface, while that of Model B was located 38 mm below the water surface. Young's modulus of the flat plates are 71 GPa, and the Poisson's ratios of the flat plates are 0.33. Table 1 summarizes the model properties. The dimensions of the wave flume were 28.962 m (length) × 0.6 m (breadth) × 0.5 m (water depth). To measure the strains, 5 or 6 strain gauges were attached to two flat plates, as shown in Figure 1.

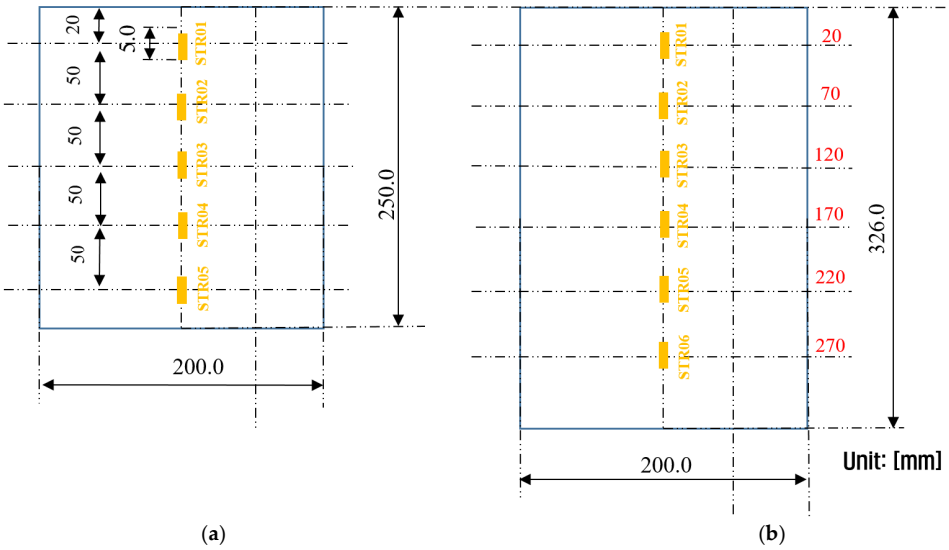

Figure 1. Experimental models and sensor locations: (**a**) Model A; (**b**) Model B.

2.2. Wave Condition

In this study, wave impact tests were conducted in breaking waves, and breaking waves were generated using the focusing wave method. As shown in Figure 2, the wave approaches the wave probe, and the high wave is broken near the wave probe. In addition, the wave has a curling shape at the moment of breaking. Figure 3 shows the wave elevations obtained from five repetitive tests. The waves generated by the five repetitive tests were in good agreement with each other. Furthermore, it can be observed that the maximum wave heights were about 0.16 m.

Table 1. Summary of the model properties.

Experimental Model	Length	Thickness	Width	Bottom Height	Young's Modulus	Poisson's Ratio
Model A	250 mm	1 mm	200 m	38 mm above water surface	71 GPa	0.33
Model B	326 mm			38 mm below water surface		

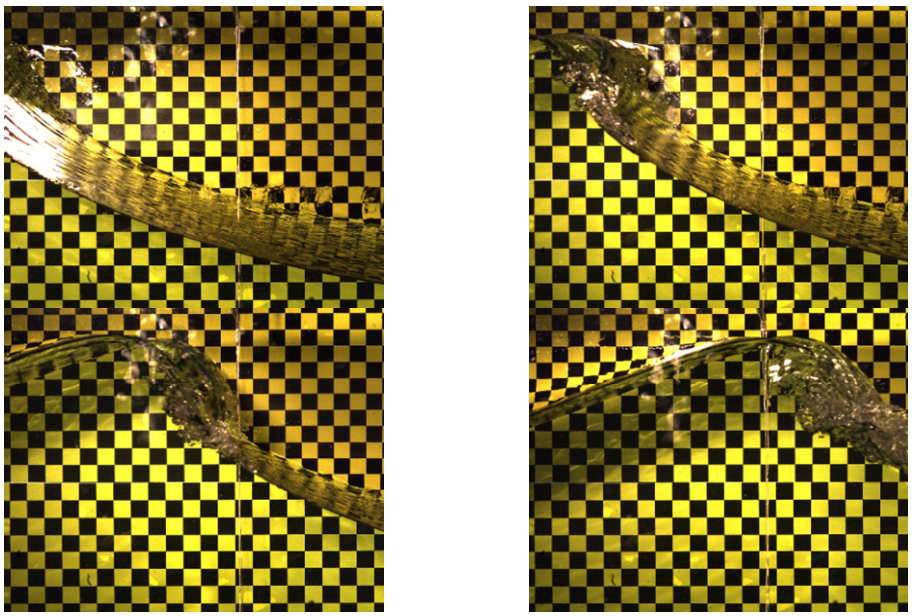

Figure 2. Snapshots for the breaking waves.

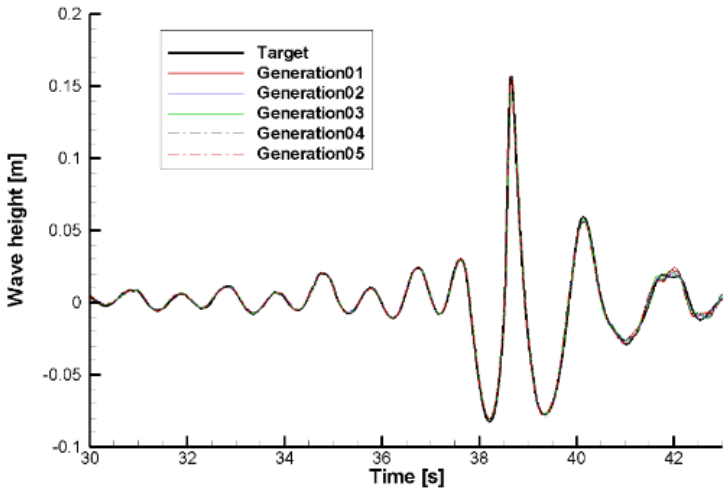

Figure 3. Wave elevations of breaking waves.

2.3. Measuring System

In this model test, the sensors were divided into two different sampling rates, as shown in Figure 4. The wave was measured at a low sampling rate of 50 Hz, and the strains were measured at a high sampling rate of 4000 Hz. The strain-gauges used were NMB B-FAE-5-12 T11 W3 of MINEBEA Co., Ltd. (Tokyo, Japan). To synchronize the measuring sensors, the NI cDAQ-9137 was used in this study. The natural frequency of the DAQ (Data Acquisition) system is formed at multiples of 60 Hz.

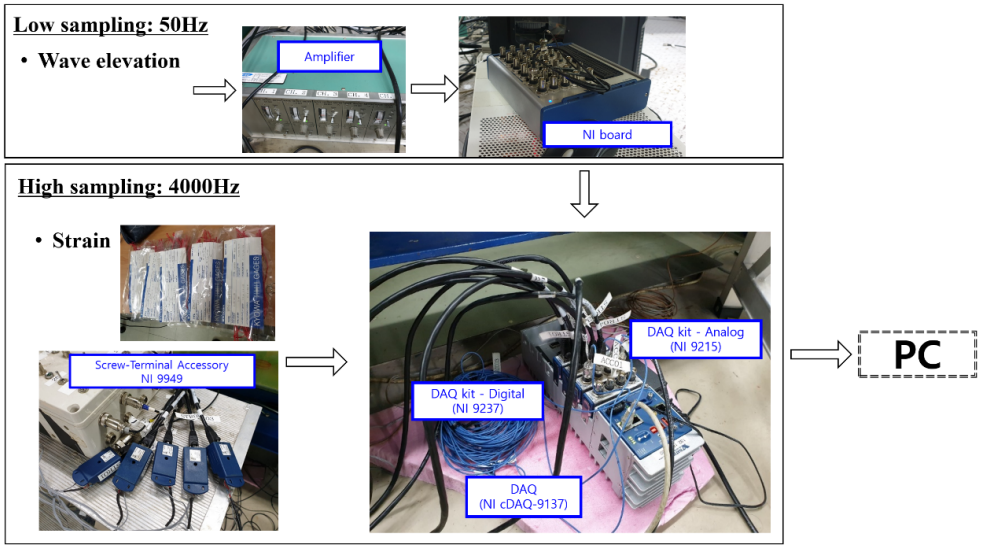

Figure 4. Experimental DAQ system.

A high speed camera (2000 frame/sec) was used to capture the flow characteristics of the breaking wave, as shown in Figure 5. In addition, the breaking waves were measured at 1 m locations in the front and back of the flat plates. Figure 6 shows the experimental model with the attached measuring instruments and its installation at the 2D wave flume. Despite the accelerometers being installed and utilized in the experiments, there was excessive noise in the experimental data. Therefore, the acceleration results were excluded from this study.

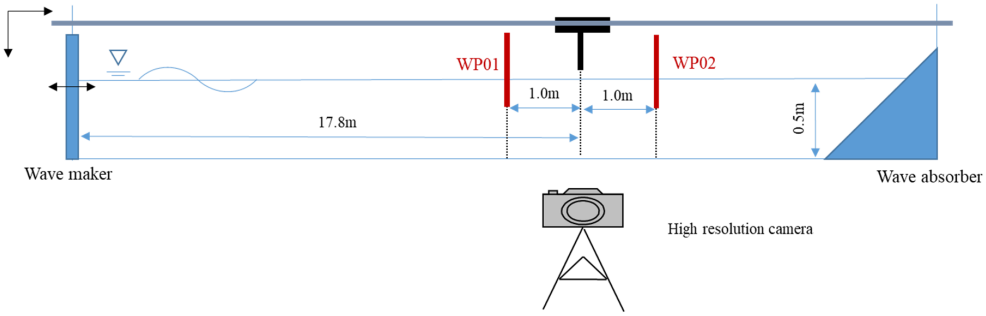

Figure 5. Experimental setup.

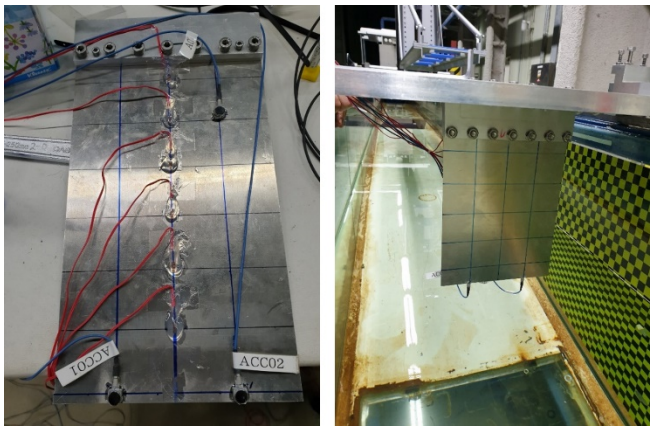

Figure 6. Experimental model with measuring instruments and its installation setup.

3. Experimental Results

3.1. Hammering Test

In this study, hammering tests were performed using an impact hammer. The impact hammer was the integrated electronics piezo-electric (IEPE) type and the KISTLER 9722 models. The natural frequency of the impact hammer is 8200 Hz. Figure 7 shows the hammering locations.

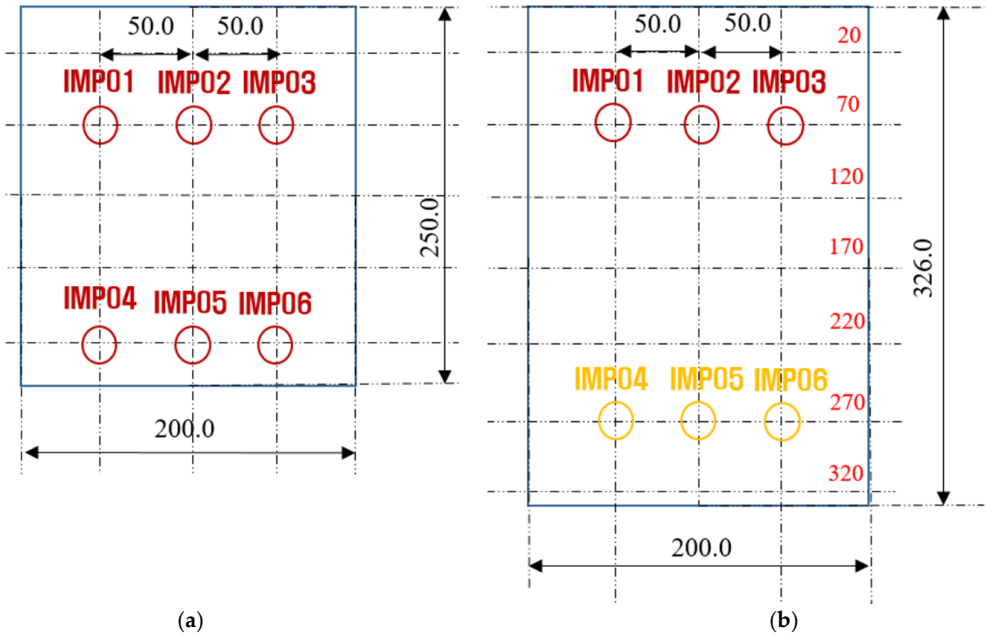

Figure 7. Hammering locations: (**a**) Model A; (**b**) Model B.

Hammering tests were performed at six different locations on the flat plates. As for Model A, the hammering tests were exclusively performed under dry conditions, while for Model B, they were performed under dry and partially wet conditions. Therefore, hammering tests in partially wet conditions could not be performed at the IMP04, IMP05 and IMP06 locations in the case of Model B.

Figure 8 shows representative snapshots of the hammering tests for Model A under dry conditions. Model A oscillates after the impact hammer hits in Model A. The hammering tests were performed three times at each location. Figure 9 shows the time histories of the strain-gauges from the hammering tests for Model A under dry conditions. It can be observed that oscillations with various frequencies occur, and oscillation characteristics are clearly measured at IMP02.

Figure 10 shows the FFT (Fast Fourier Transform) results of the hammering tests on Model A under dry conditions. As shown in Figure 10a,c, the energies at two frequencies are clearly captured near 10 Hz and 75 Hz however, the energies in the frequency near 75 Hz are relatively small, as shown in Figure 10b,d. It can be observed that the hammering test results depend on the hitting points. To validate the experimental results, modal analyses for Model A were performed using the ANSYS program. Figure 11 shows the mode shapes obtained by modal analyses.

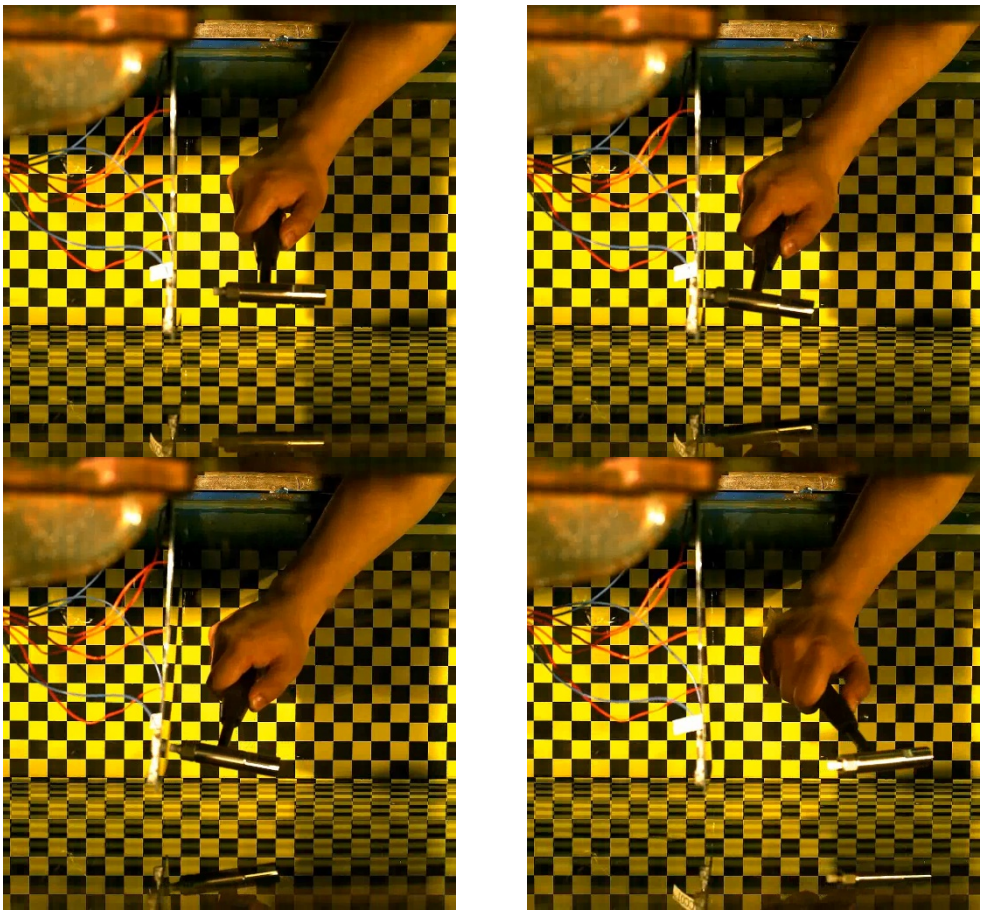

Figure 8. Snapshots for the hammering tests (Model A, Dry condition).

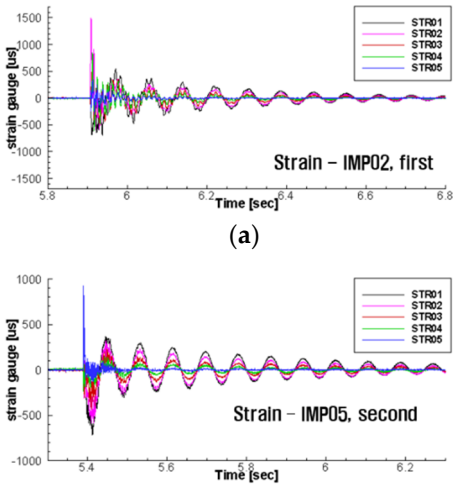

Figure 9. Time histories for strain-gauges from the hammering tests on Model A in dry condition: (**a**) First test, IMP02 location; (**b**) second test, IMP05 location.

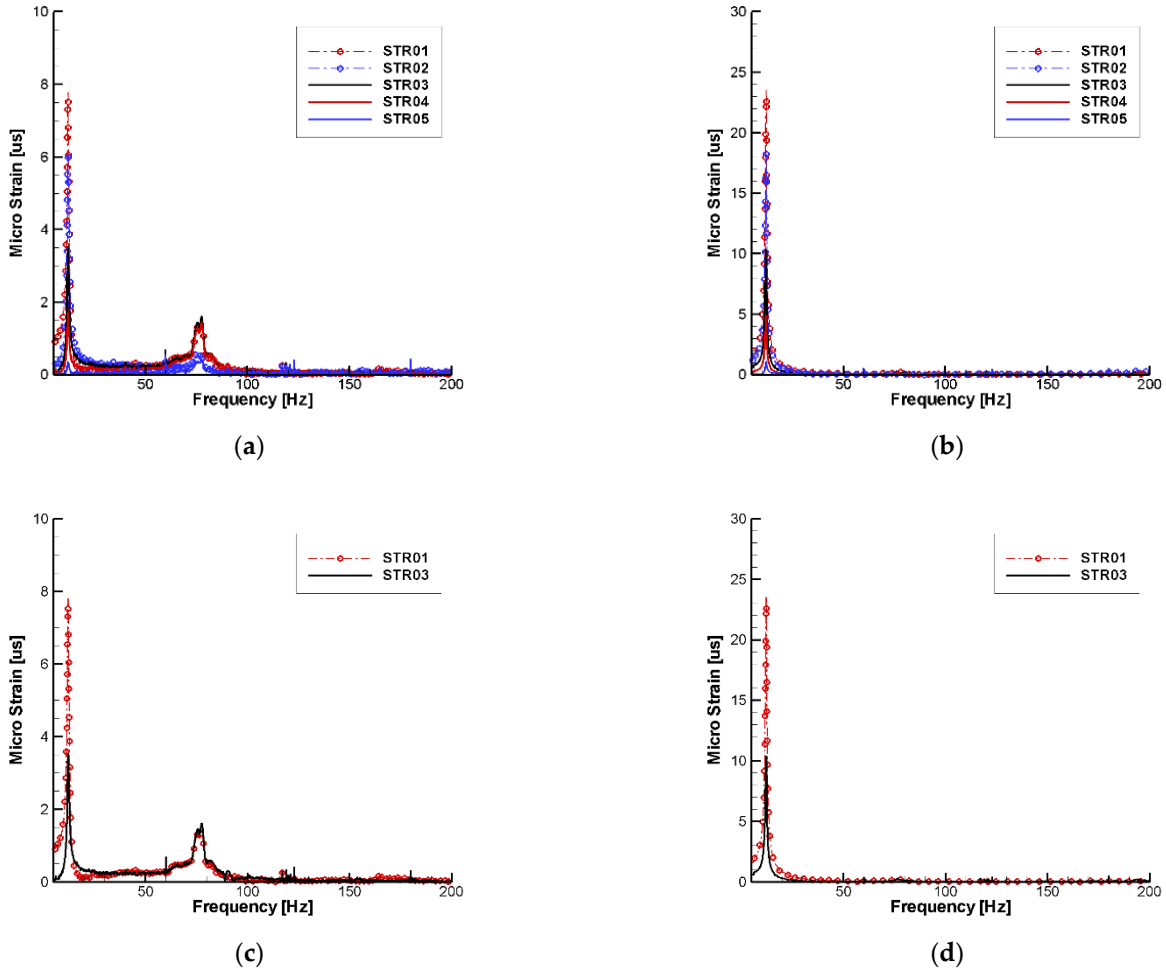

Figure 10. FFT results of the hammering tests on Model A in dry condition: (**a**) first test, IMP02 location; (**b**) second test, IMP05 location; (**c**) first test, IMP02 location (STR01, STR03); (**d**) second test, IMP05 location (STR01,STR03).

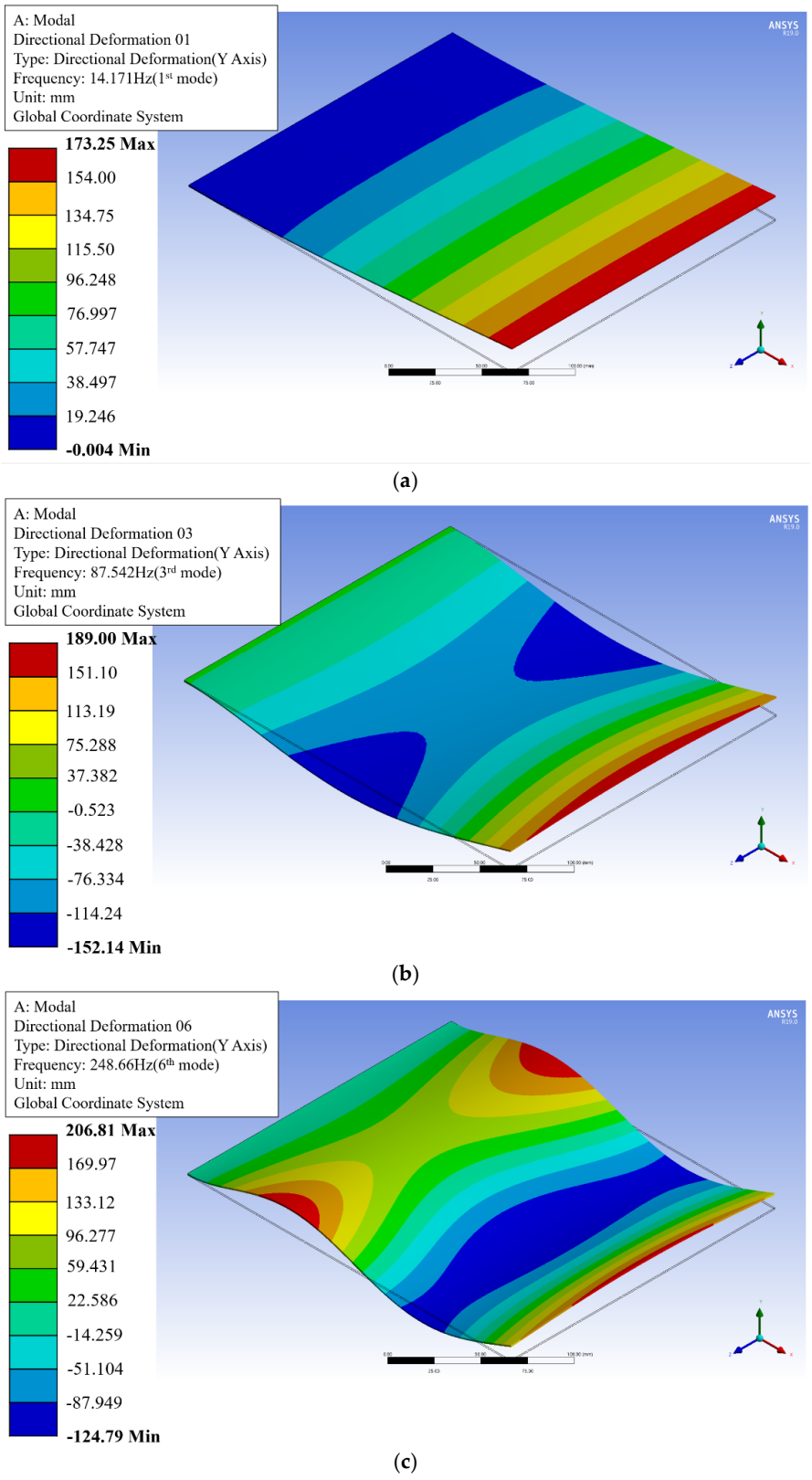

Figure 11. Modal analysis results by ANSYS program: (**a**) 1st mode (**b**) 3rd mode; (**c**) 6th mode.

The hammering test results were directly compared with the modal analysis results, as shown in Figure 12. The frequencies near 10 Hz and 75 Hz in Figure 10 are the 1st and 3rd modes, respectively. As shown in Figure 12a, the frequencies in 1st mode between

the hammering tests and modal analyses are slightly different. The differences can occur due to the slight mass differences, such as sensor lines, attached sensors, etc. In addition, the frequencies in the 3rd mode are strongly affected by the mass differences, as shown in Figure 12b.

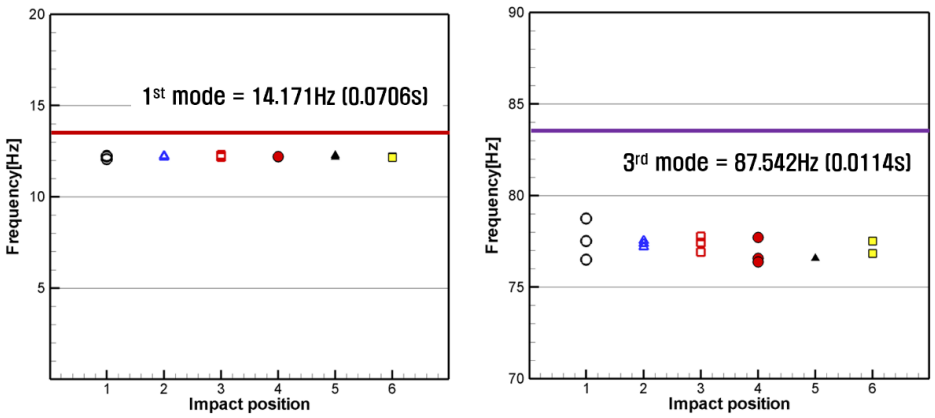

(**a**) (**b**)

Figure 12. Frequencies for each mode of Model A in dry condition: (**a**) 1st mode; (**b**) 3rd mode.

For Model B, hammering tests were performed under dry and partially wet conditions. Figure 13 shows representative snapshots of the hammering tests under partially wet conditions. It can be observed that Model B oscillates with water after the impact hammer hits on Model B. Figure 14 shows the FFT results of the hammering tests on Model B under dry and partially wet conditions. In the partially wet condition, due to the additional water mass, the frequencies in each mode are moved to the low frequency regions compared to the results in dry conditions. Figure 15 shows the comparison results between the dry and partially wet conditions for each mode. As shown in Figure 15a, the 1st mode frequency of 7.968 Hz in the dry condition becomes smaller than 1st mode frequency of 2.803 Hz under the partially wet conditions. The difference in the 1st mode frequencies between the dry and partially wet conditions is 64.8%. As for the 3rd mode frequency, the difference between the dry and partially wet conditions is 19.8%, as shown in Figure 15b. Under dry conditions, the 6th mode was difficult to capture; thus the 5th mode in the dry condition was compared with the 6th mode in the partially wet condition. In spite of the 5th mode in the dry condition, the frequency is relatively higher than the 6th mode frequency in the partially wet condition.

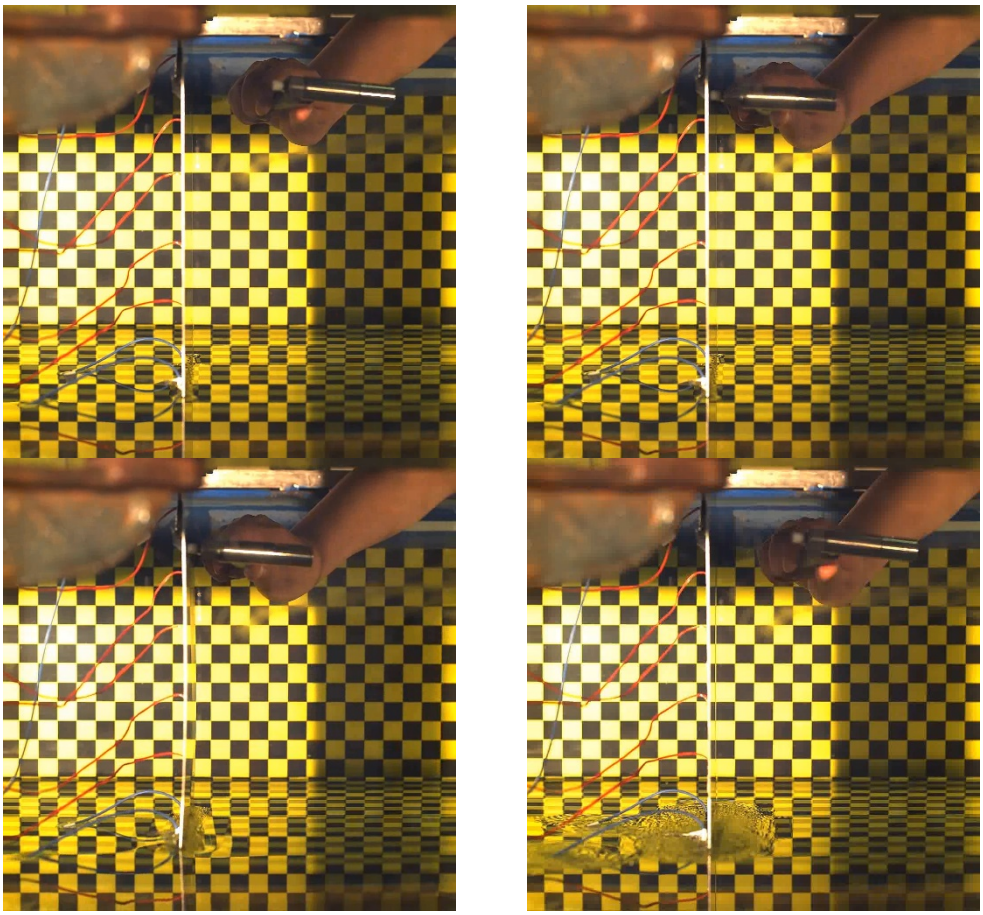

Figure 13. Snapshots for the hammering tests (Model B, partially wet condition).

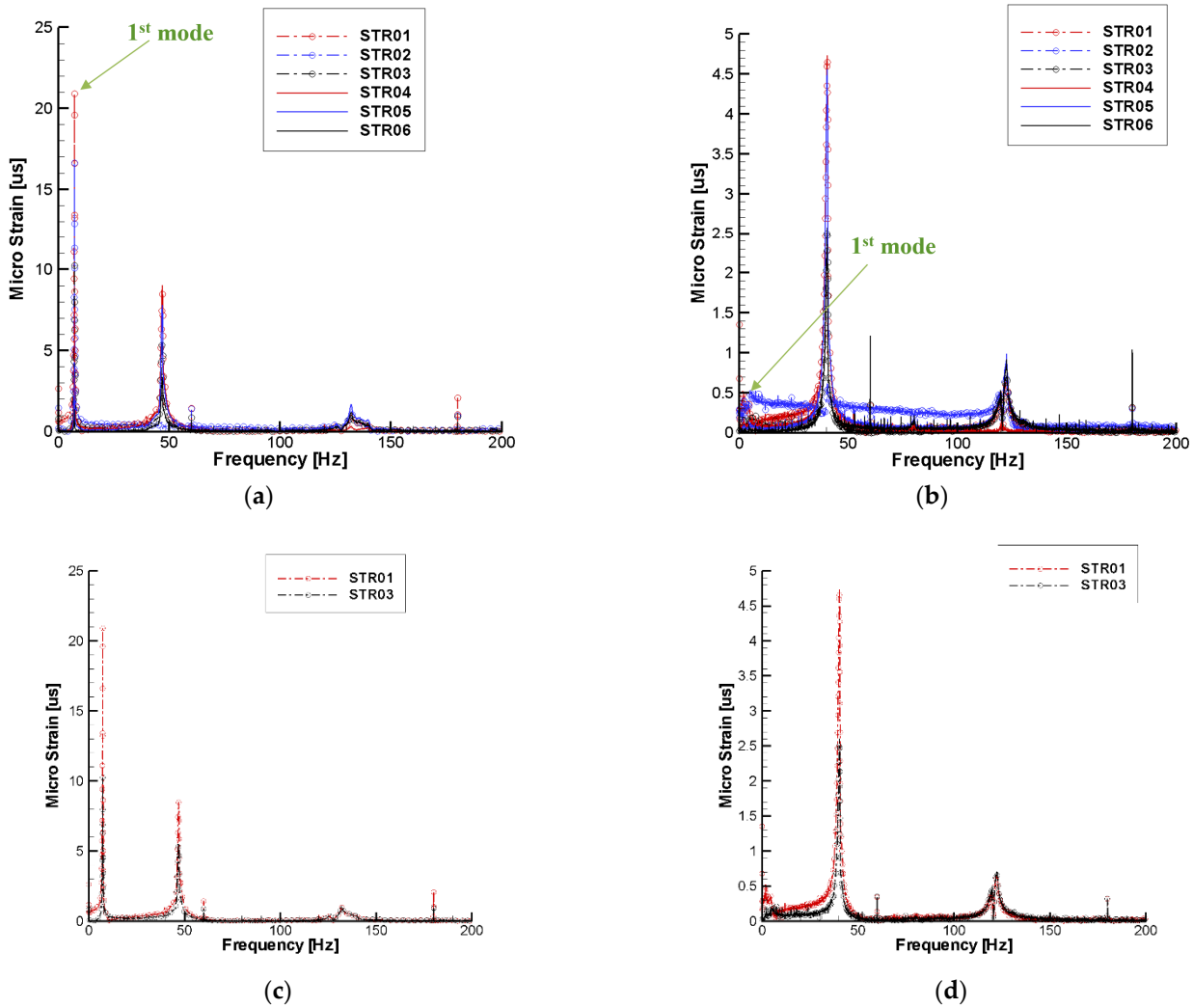

Figure 14. FFT results of the hammering tests on Model B in dry and partially wet conditions: (**a**) dry condition, IMP02 location; (**b**) partially wet condition, IMP02 location; (**c**) dry condition, IMP02 location (STR01, STR03); (**d**) partially wet condition, IMP02 location (STR01, STR03).

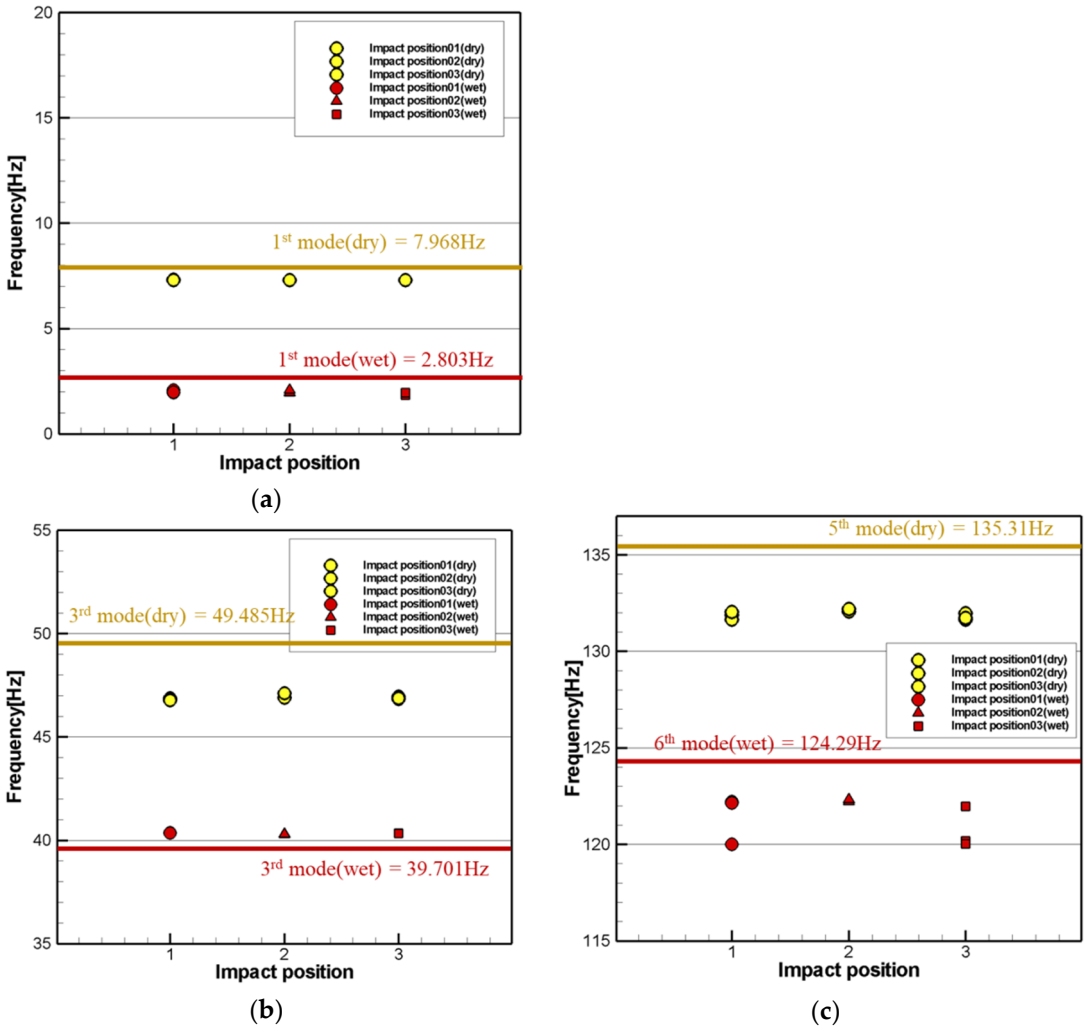

Figure 15. Frequencies for each mode of Model B in dry and partially wet condition: (**a**) 1st mode; (**b**) 3rd mode; (**c**) 5th and 6th modes.

3.2. Breaking Wave Test

In this study, breaking wave tests on Models A and B were performed. Figure 16 shows representative snapshots of the breaking wave tests for Model A. The breaking wave approaches Model A, and the breaking wave with a curling shape strongly hits Model A. Thereafter, Model A is inclined. This phenomenon can be understood as a hammering test by breaking waves. In this study, four repetitive tests were performed for each model. Figure 17 shows the representative time histories of the strain-gauges in the 1st breaking wave test for Model A. It can be observed that the strains occur near 38 s, because the wave components are focused near 38 sec, as shown in Figure 3. In addition, the strains obtained by the repetitive tests are in good agreement with each other.

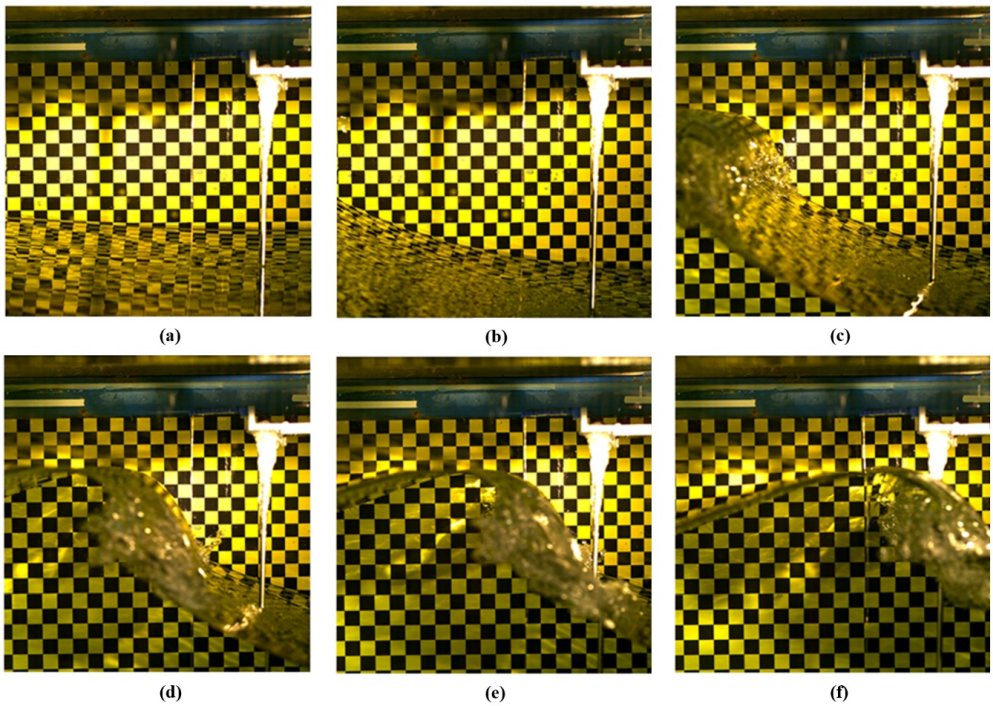

Figure 16. Sequential wave snapshots from (**a**–**f**) of breaking wave tests for Model A (dry condition).

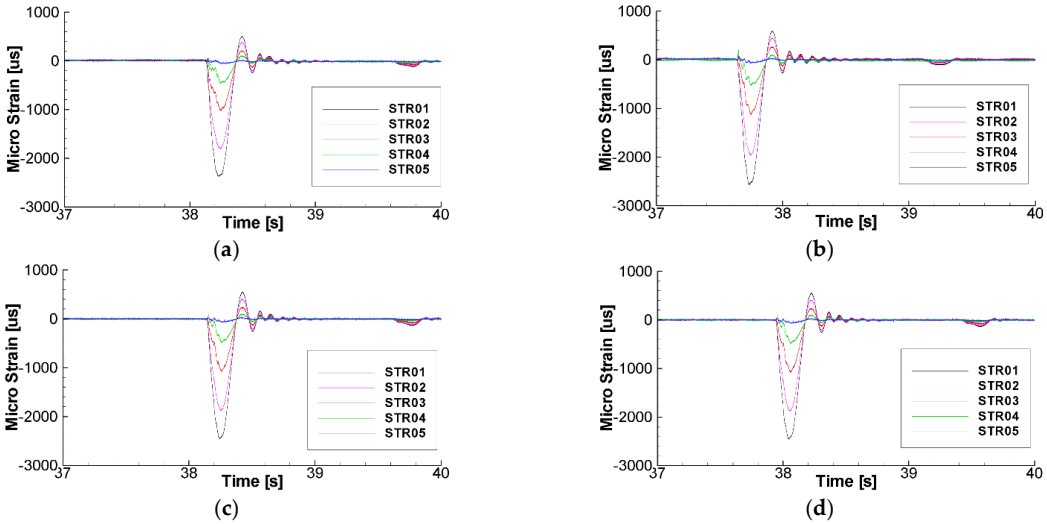

Figure 17. Time histories of the strain-gauges by 4 repetitive tests under the breaking waves (Model A, dry condition): (**a**) 1st test, (**b**) 2nd test, (**c**) 3rd test, (**d**) 4th test.

Figure 18 shows the representative FFT results for the time histories of the strain-gauges and waves under the breaking waves, and it can be seen that the wave frequencies dominate. As shown in Figure 18a, the 3rd peak is located near 13 Hz, and it can be observed that the 3rd peak is the 1st mode of Model A. As for the 2nd peaks near 7 Hz, they seem to be frequencies of air bubbles by trapped air in breaking waves. Figure 19 shows the time histories of the strain-gauges in Model B under breaking waves. For Model B, breaking wave tests were performed under partially wet conditions. The results of the four repetitive tests are in good agreement with each other. It can be observed that Model B oscillates with incoming waves before the wave impact. In addition, the relatively long oscillation by wave impact occurs in Model B, and Model B oscillates shortly after the wave impact.

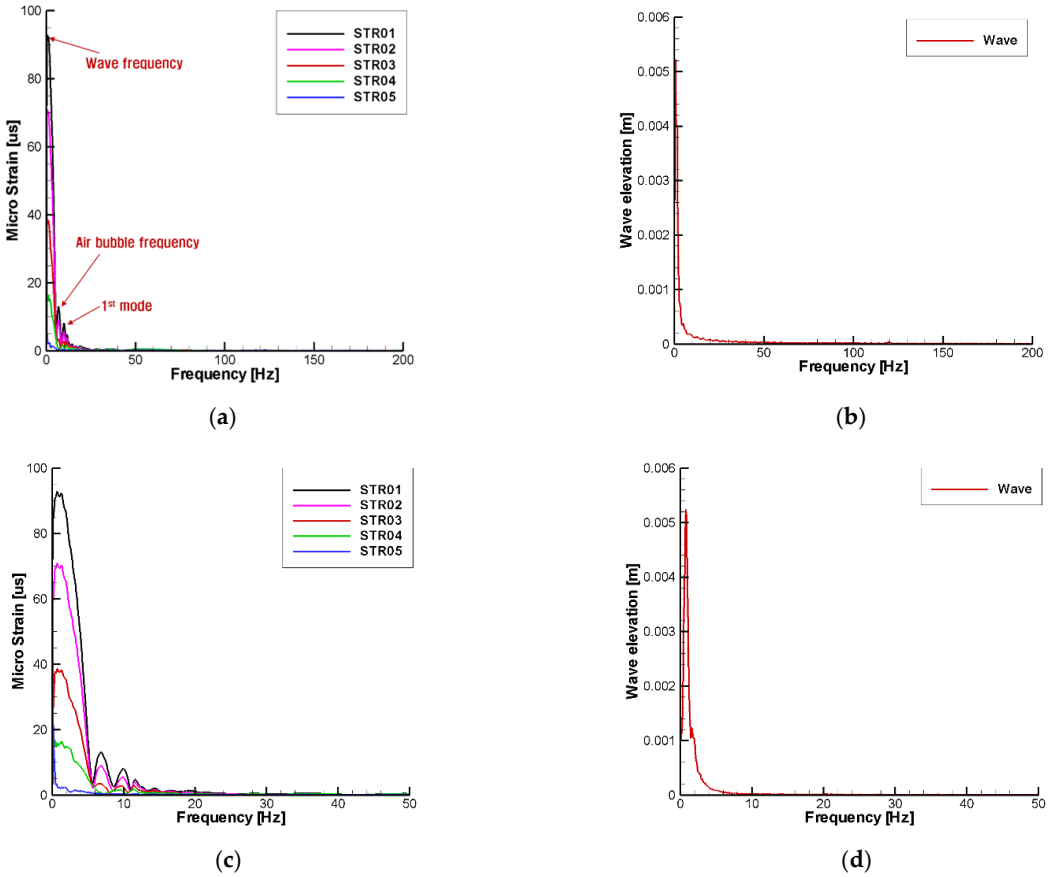

Figure 18. Representative FFT results for time histories of the strain-gauges and waves under the breaking waves (Model A, dry condition, 1st test): (**a**) strain-gauge signals, (**b**) wave elevation; (**c**) strain-gauge signals (close-up), (**d**) wave elevation (close-up).

Figure 20 shows the representative FFT results for the time histories of the strain-gauges in Figure 19a. In common with Model A, the wave frequencies occur near 0.6 Hz, and it can be also seen that the air bubble frequencies occur near 7 Hz. In addition, it can be observed that the frequencies of the 1st mode occur near 3 Hz. Interestingly, the frequencies of the 3rd and 6th modes occur in the case of Model B. From the breaking wave tests, the mode shapes can be captured to be similar to the hammering tests, and it can be found that the wave and air bubble frequencies are captured.

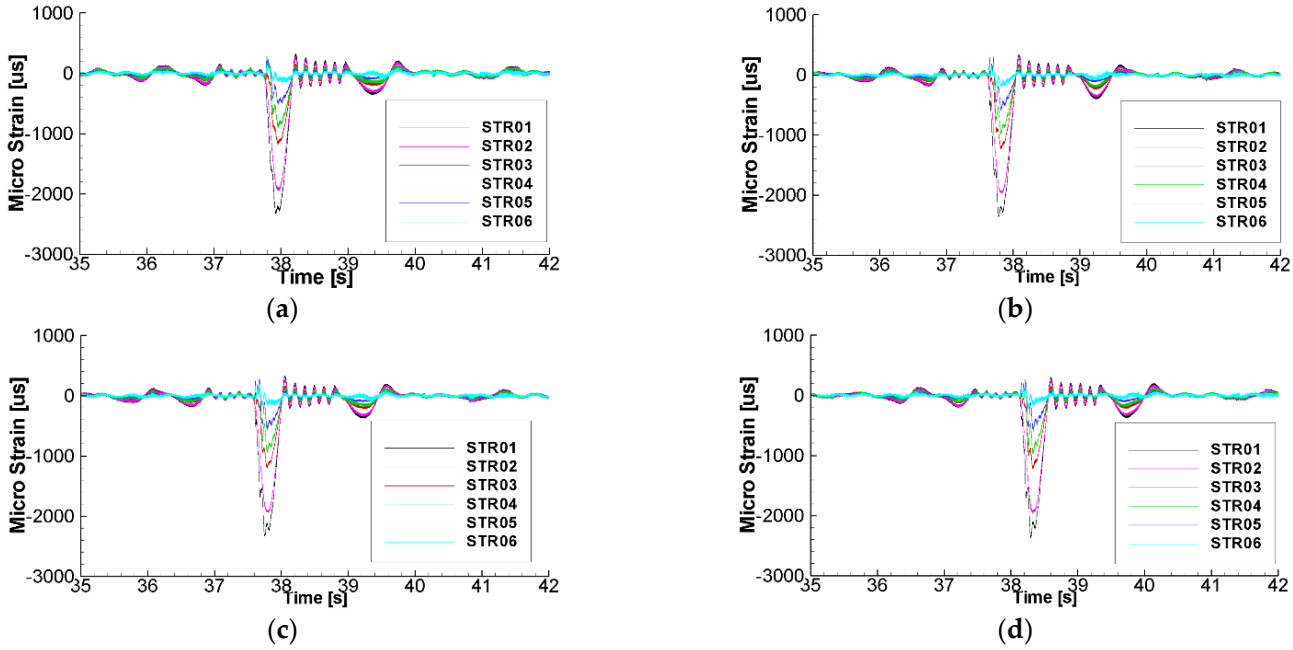

Figure 19. Time histories of the strain-gauges by 4 repetitive tests under the breaking waves (Model B, partially wet condition): (**a**) 1st test, (**b**) 2nd test, (**c**) 3rd test, (**d**) 4th test.

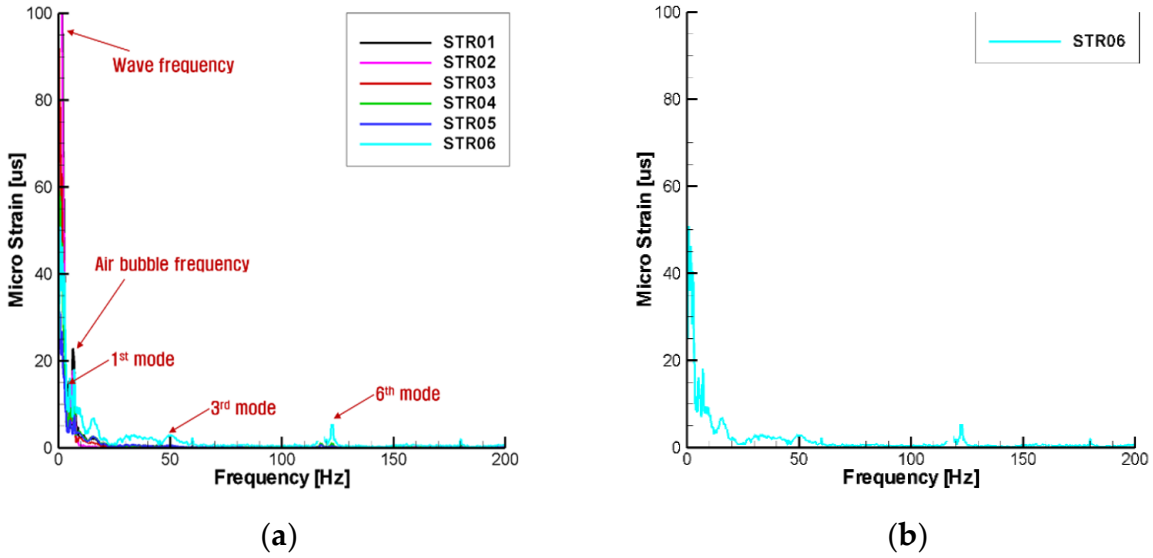

Figure 20. Representative FFT results for time histories of the strain-gauges under the breaking waves (Model B, partially wet condition, 1st test): (**a**) all data, (**b**) STR06.

Figure 21 shows the strains with standard deviations for 1st peaks of Figures 17 and 19. It can be observed that the standard deviations are small, and thus the experimental results show good repeatability. Figure 22 shows the time intervals between the 1st negative peaks and 2nd positive peaks in Figures 17 and 19. To validate the numerical simulation, the data shown in Figures 21 and 22 can be useful.

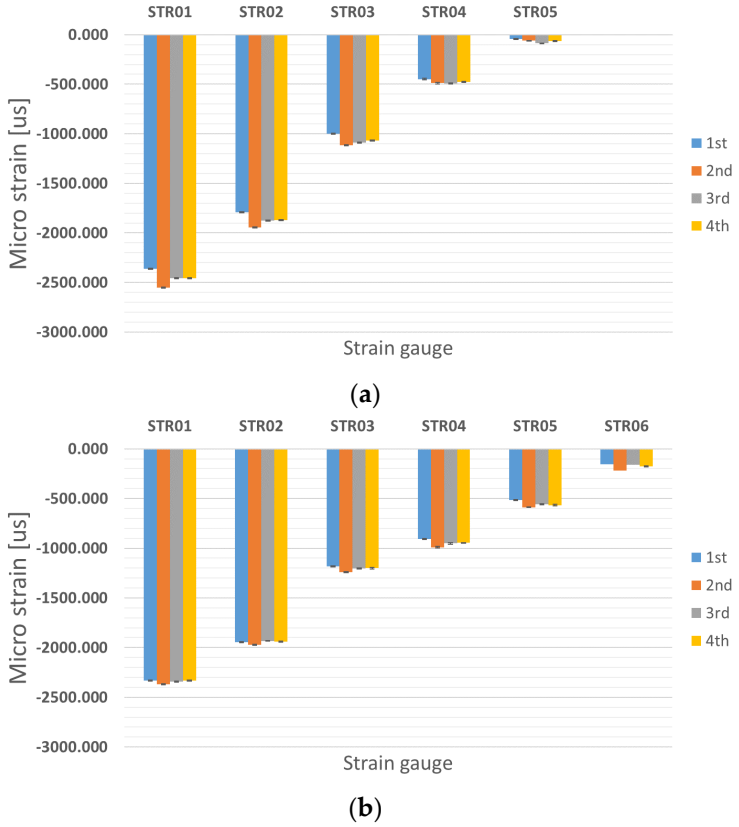

Figure 21. Strains with standard deviations for 1st peaks by breaking wave tests: (**a**) Model A, (**b**) Model B.

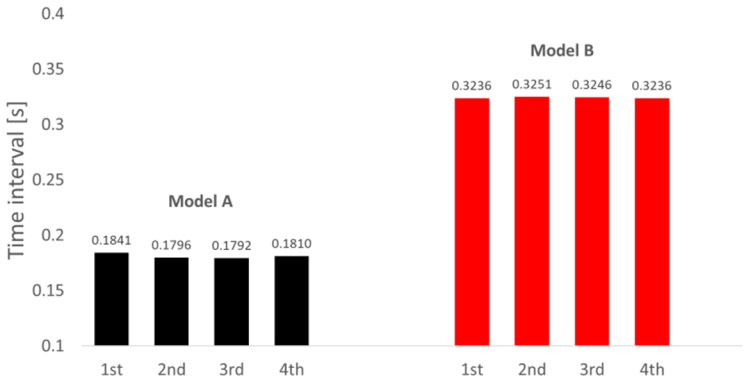

Figure 22. Time intervals of strains for 1st peaks by breaking wave tests.

4. Conclusions

In this study, the results from a series of model tests for the validation data of a numerical simulation are presented for two flat plates. From the experiments, the frequencies of each mode and the strains are suggested.

(1) From the hammering tests under dry conditions, the frequencies of the 1st and 3rd modes for Model A occur near 13 Hz and 78 Hz, respectively. In addition, the repetitive data on the IMP02 location show good agreement with each other.

(2) For Model B, hammering tests were performed under dry and partially wet conditions. Thus, the frequencies in each mode under partially wet conditions are moved to the low-frequency regions compared to the results in the dry condition.

(3) In the breaking wave test, for Model A, the wave frequency dominantly occurs, and the 1st mode can be captured. In addition, the air bubble frequency between the wave and 1st mode frequencies occurs, and the air bubble frequency is near 7 Hz. The air bubble frequency near 7 Hz occurred in the model tests for Model B as well.
(4) It can be observed that the frequencies of the 1st, 3rd and 6th modes of Model B occur under the breaking waves. Therefore, the frequencies in each mode can be captured to be similar to the hammering tests. The wave and air bubble frequencies were additionally captured from the breaking wave tests.
(5) Quantitative data, such as the strain and time interval of the measured data peaks, are provided, and the data can be useful for the validation of a numerical simulation.

Author Contributions: Conceptualization, Y.-H.K. and Y.-J.H.; methodology, Y.-H.K. and Y.-J.H.; software, Y.-H.K. and B.-J.P.; validation, Y.-H.K. and Y.-J.H.; formal analysis, Y.-H.K. and B.-J.P.; investigation, Y.-H.K. and B.-J.P.; resources, Y.-H.K. and B.-J.P.; data curation, Y.-H.K. and B.-J.P.; writing—original draft preparation, Y.-J.H.; writing—review and editing, Y.-H.K.; visualization, Y.-H.K. and B.-J.P.; supervision, Y.-H.K. and Y.-J.H.; project administration, Y.-H.K. and Y.-J.H.; funding acquisition, B.-J.P. and K.-S.L. All authors have read and agreed to the published version of the manuscript.

Funding: This research was funded by the National R&D Project, grant number PMS4700 and by Korea Research Institute of Ships and Ocean Engineering, grant number PES3490.

Institutional Review Board Statement: Not applicable.

Informed Consent Statement: Not applicable.

Data Availability Statement: Not applicable.

Acknowledgments: This study was supported by a grant from the National R&D Project "Development of an electric-powered car ferry and a roll-on/roll-off power supply system" funded by the Ministry of Oceans and Fisheries, Korea (PMS4700)", and a grant from the Endowment Project "Core Technology Development of Hydro-elasticity based Structural Damage Assessment for Offshore Structures considering Uncertainty (PES3490)". The authors especially thank the KRISO ocean engineering basin technicians for their dedicated efforts.

Conflicts of Interest: The authors declare no conflict of interest.

References

1. Newman, J.N. Wave effects on deformable bodies. *Appl. Ocean Res.* **1994**, *16*, 47–59. [CrossRef]
2. Kjeldsen, S.P.; Torum, A.; Dean, R.G. Wave Forces on Vertical Piles Caused by 2 and 3 Dimensional Breaking Waves. In Proceedings of the 20th International Conference on Coastal Engineering, Taipei, Taiwan, 9–14 November 1986; pp. 1929–1942.
3. Basco, D.R.; Niedzwecki, J.M. Breaking wave force distributions and design criteria for slender piles. In Proceedings of the Offshore Technology Conference, Houston, TX, USA, 1–4 May 1989; pp. 425–431.
4. Hong, K.Y.; Shin, S.H. Instability of plunging breaking wave impact on inclined cylinder. *J. Korean Soc. Mar. Environ. Eng.* **2007**, *10*, 187–192.
5. von Karman, T. *The Impact on Seaplane Floats during Landing*; Technical Note 321; National Advisory Committee for Aeronautics: Washington, DC, USA, 1929.
6. Wagner, H. Über Stoß-und Gl-eitvorgänge an der oberfläche von flüssigkeiten. *Z. Angew. Math. Mech.* **1932**, *12*, 193–215. (In German) [CrossRef]
7. Goda, Y.; Haranaka, S.; Kitahata, M. *Study on Impulsive Breaking Wave Forces on Piles*; Report Port and Harbour Technical Research Institute: Kanagawa, Japan, 1966; Volume 6, pp. 1–30.
8. Hattori, M.; Arami, A.; Yui, T. Wave impact pressure on vertical walls under breaking waves of various types. *Coast. Eng.* **1994**, *22*, 79–114. [CrossRef]
9. Chan, E.S.; Cheon, H.F.; Tan, B.C. Laboratory study of plunging wave impacts on vertical cylinders. *Coast. Eng.* **1995**, *25*, 87–107. [CrossRef]
10. Wienke, J.; Sparboom, U.; Oumeraci, H. Breaking wave impact on a slender cylinder. In Proceedings of the 27th International Conference on Coastal Engineering (ICCE 2000), Sydney, Australia, 16–21 July 2000; Volume 2, pp. 1787–1798.
11. Ha, Y.J.; Kim, K.H.; Nam, B.N.; Hong, S.Y. Experimental Investigation for Characteristics of Wave Impact Loads on a Vertical Cylinder in Breaking Waves. *Ocean Eng.* **2020**, *209*, 107470. [CrossRef]

12. Huang, Z.; Spencer, D.; Oberlies, R.; Watts, G.; Xiao, W. Wave impact experiment of a GBS model in large waves. In Proceedings of the 36th International Conference on Ocean, Offshore, and Arctic Engineering, Trondheim, Norway, 25–30 June 2017. OMAE2017-61473.
13. Jose, J.; Choi, S.J. Estimation of slamming coefficients on local members of offshore wind turbine foundation (jacket type) under plunging breaker. *Int. J. Nav. Archit. Ocean Eng.* **2017**, *9*, 624–640. [CrossRef]
14. Ha, Y.J.; Kim, K.H.; Nam, B.N.; Hong, S.Y.; Kim, H.J. Experimental study for characteristics of slamming loads on bow of a ship-type FPSO under breaking and irregular wave conditions. *Ocean Eng.* **2021**, *224*, 108738. [CrossRef]
15. Chuang, S.L. *Investigation of Impact of Rigid and Elastic Bodies with Water*; NSR & DC Report 3248; ProQuest Dissertations Publishing: Morrisville, CA, USA, 1970.
16. Moragues, M.V.; Clavero, M.; Losada, M.A. Wave breaker types on a smooth and impermeable 1:10 slope. *J. Mar. Sci. Eng.* **2020**, *8*, 296. [CrossRef]
17. Li, C.; Gao, F.; Yang, L. Breaking-wave induced transient pore pressure in a sandy seabed: Flume modeling and observations. *J. Mar. Sci. Eng.* **2021**, *9*, 160. [CrossRef]
18. Escudero, M.; Hernandez-Fontes, J.V.; Hernandez, I.D.; Mendoza, E. Virtual level analysis applied to wave flume experiments: The case of waves-cubipod homogeneous low-crested structure interaction. *J. Mar. Sci. Eng.* **2021**, *9*, 230. [CrossRef]
19. Khayyer, A.; Gotoh, H. A multiphase compressible-incompressible particle method for water slamming. *Int. J. Offshore Polar Eng.* **2016**, *26*, 20–25. [CrossRef]
20. Liu, P.L.-F.; Lin, P.; Chang, K.-A.; Sakakiyama, T. Wave interaction with porous structures. *J. Waterw. Port. Coastal. Ocean Eng.* **1999**, *125*, 322–330. [CrossRef]
21. Kamath, A.; Chella, M.A.; Bihs, H.; Arntsen, O.A. Breaking wave interaction with a vertical cylinder and the effect of breaker location. *Ocean Eng.* **2016**, *128*, 105–115. [CrossRef]
22. Ha, Y.J.; Kim, K.H.; Nam, B.N.; Hong, S.Y. CFD simulation of wave impact loads on a truncated circular cylinder by breaking waves. *Int. J. Offshore Polar Eng.* **2019**, *29*, 306–314. [CrossRef]
23. Fu, S.; Moan, T.; Chen, X.; Cui, W. Hydroelastic analysis of flexible floating interconnected structures. *Ocean Eng.* **2007**, *34*, 1516–1531. [CrossRef]
24. Hamamoto, T.; Fujita, K. Wet-mode superposition for evaluating the hydroelastic response of floating structures with arbitrary shape. In Proceedings of the International Offshore and Polar Engineering Conference, Kitakyushu, Japan, 26–31 May 2002; Volume 12, pp. 290–297.
25. Wu, H.L.; Chen, X.J.; Shen, H.P.; Wu, Y.S. Experimental and numerical investigation of the hydroelasticity of a floating structure with legs. *Mar. Struct.* **2018**, *61*, 100–118. [CrossRef]
26. Malenica, S.; Molin, B.; Remy, F.; Sejanović, I. *Hydroelastic Response of a Barge to Impulsive and Non-Impulsive Wave Loads*; The Oxford University: Oxford, UK, 2003; pp. 107–116.
27. Kara, F. Time domain prediction of hydroelasticity of floating bodies. *Appl. Ocean Res.* **2015**, *51*, 1–13. [CrossRef]
28. Rajendran, S.; Soares, C.G. Numerical investigation of the vertical response of a containership in large amplitude wave. *Ocean Eng.* **2016**, *123*, 440–451. [CrossRef]
29. Sejanović, I.; Malenica, Š.; Tomašević, S. Investigation of ship hydroelasticity. *Ocean Eng.* **2008**, *35*, 523–535. [CrossRef]
30. Loukogeorgaki, E.; Michailides, C.; Angelides, D.C. Dry and wet mode superposition approaches for the hydroelastic analysis of floating structures. In Proceedings of the International Conference on Structural Dynamic, Porto, Portugal, 30 June–2 July 2014; pp. 3089–3096.
31. Michailides, C.; Loukogeorgaki, E.; Angelides, D.C. Response analysis and optimum configuration of a modular floating structure with flexible connectors. *Appl. Ocean Res.* **2013**, *43*, 112–130. [CrossRef]
32. Fourey, G.; Hermange, C.; Le Touzé, D.; Oger, G. An efficient FSI coupling strategy between smoothed particle hydrodynamics and finite element methods. *Comput. Phys. Commun.* **2017**, *217*, 66–81. [CrossRef]
33. Li, Z.; Leduc, J.; Nunez-Ramirez, J.; Combescure, A.; Marongiu, J.C. A non-intrusive partitioned approach to couple smoothed particle hydrodynamics and finite element methods for transient fluid-structure interaction problems with large interface motion. *Comput. Mech.* **2015**, *55*, 697–718. [CrossRef]
34. Liu, M.; Zhang, Z. Smoothed particle hydrodynamics (SPH) for modeling fluid-structure interactions. *Sci. China Phys. Mech. Astron.* **2019**, *62*, 984701. [CrossRef]
35. Sun, Z.; Zhang, G.; Zong, Z.; Djidjeli, K.; Xing, J. Numerical analysis of violent hydroelastic problems based on a mixed MPS-mode superposition method. *Ocean Eng.* **2019**, *179*, 285–297. [CrossRef]
36. Izadi, M.; Ghadimi, P.; Fadavi, M.; Tavakoli, S. Hydroelastic analysis of water impact of flexible asymmetric wedge with an oblique speed. *Meccanica* **2018**, *53*, 2285–2617. [CrossRef]
37. Liao, K.; Hu, C.; Duan, W. Two-dimensional numerical simulation of an elastic wedge water entry by a coupled FDM-FEM method. *J. Mar. Sci. Appl.* **2013**, *12*, 163–169. [CrossRef]
38. Donea, J.; Jiuliani, S.; Halleux, J.P. An arbitrary lagrangian-eulerian finite element method for transient dynamic fluid-structure interactions. *Comput. Method. Appl. Mech. Eng.* **1982**, *33*, 689–723. [CrossRef]
39. Hirt, C.W.; Amsden, A.A.; Cook, J.L. An arbitrary lagrangian-eulerian computing method for all speeds. *J. Comp. Phys.* **1974**, *14*, 227–253. [CrossRef]

40. Hughes, T.J.R.; Liu, W.K.; Zimmerman, T. Lagrangian-eulerian finite element formulation for incompressible viscous flow. *Comput. Method. Appl. Mech. Eng.* **1981**, *29*, 329–349. [CrossRef]
41. Hu, H.H.; Patankar, N.A.; Zhu, M.Y. Direct numerical simulations of fluid-solid systems using the arbitrary lagrangian-eulerian technique. *J. Comp. Phys.* **2001**, *20*, 427–462. [CrossRef]
42. Peskin, C.S.; McQueen, D.M. A three-dimensional computational method for blood flow in the heart I. Immersed elastic fibers in a viscous incompressible fluid. *J. Comp. Phys.* **1989**, *81*, 372–405.
43. Dillion, R.; Fauci, L.J. An integrative model of internal axoneme mechanics and external fluid dynamics in ciliary beating. *J. Theor. Biol.* **2002**, *207*, 415–430. [CrossRef]
44. Gilmanov, A.; Sotiropoulos, F. A hybrid cartesian/immersed boundary method for simulating flows with 3D, geometrically complex, moving bodies. *J. Comp. Phys.* **2005**, *207*, 457–492. [CrossRef]
45. Zhu, L.; Peskin, C.S. Simulation of a flapping flexible filament in a flowing soap film by the immersed boundary method. *J. Comp. Phys.* **2002**, *179*, 452–468. [CrossRef]
46. Nestola, M.G.C.; Becsek, B.; Zolfaghari, H.; Zulian, P.; Marinis, D.D.; Krause, R.; Obrist, D. An immersed boundary method for fluid-structure interaction based on overlapping domain decomposition. *J. Comput. Physics.* **2019**, *398*, 108884. [CrossRef]
47. Griffith, B.E.; Patankar, N.A. Immersed methods for fluid structure interaction. *Annu. Rev. Fluid Mech.* **2020**, *52*, 421–448. [CrossRef]
48. Glowinski, R.; Pan, T.-W.; Periaux, J. A lagrange multiplier/fictitious domain method for the numerical simulation of incompressible viscous flow around moving rigid bodies: (I) case where the rigid body motions are known a priori. *C. R. Acad. Sci. Paris* **1997**, *25*, 361–369. [CrossRef]
49. van Loon, R.; Anderson, P.D.; de Hart, J.; Baaijens, F.P.T. A combined fictitious domain/adaptive meshing method for fluid-structure interaction in heart valves. *Int. J. Numer. Methods Fluids* **2004**, *46*, 533–544. [CrossRef]
50. Kim, K.H.; Kim, B.W.; Hong, S.Y. Experimental investigations on extreme bow-flare slamming loads of 10,000-TEU containership. *Ocean Eng.* **2019**, *171*, 225–240. [CrossRef]
51. Garabedian, P.R. Oblique water entry of a wedge. *Commun. Pure Appl. Math.* **1953**, *6*, 157–165. [CrossRef]
52. Judge, C.; Troesch, A.; Perlin, M. Initial water impact of a wedge at vertical and oblique angles. *J. Eng. Math.* **2004**, *48*, 279–303. [CrossRef]
53. Barjasteh, M.; Zeraatgar, H.; Javaherian, M.J. An experimental study on water entry of asymmetric wedges. *Appl. Ocean Res.* **2016**, *58*, 292–304. [CrossRef]
54. Russo, S.; Jalalisendi, M.; Falcucci, G.; Porfiri, M. Experimental characterization of oblique and asymmetric water entry. *Exp. Therm. Fluid Sci.* **2018**, *92*, 141–161. [CrossRef]
55. Wang, S.; Guedes Soares, C. Asymmetrical water impact of two-dimensional wedges with roll angle. *Int. J. Marit. Eng.* **2014**, *156*, 115–130.